

LOW ENERGY ELECTRON DIFFRACTION STUDY OF  
EPITAXIAL  $\text{Cr}_2\text{O}_3(0001)$  FILMS GROWN ON  $\text{Cr}(110)$

HONORS THESIS

Presented to the Honors Committee of

Texas State University-San Marcos

In Partial Fulfillment of

the Requirements

For Graduation in the University Honors Program

By

Sy Redding

San Marcos, Texas

May 2009

# Table of Contents

<b>List of Figures</b> .....	<b>iii</b>
<b>List of Tables</b> .....	<b>iv</b>
<b>Acknowledgements</b> .....	<b>v</b>
<b>Abstract</b> .....	<b>vi</b>
<b>I. Introduction</b> .....	<b>1</b>
<b>II. Theoretical Approach</b> .....	<b>3</b>
II. A. Construction of the Reciprocal Lattice for Chromium(110).....	7
II. B. Construction of the Reciprocal Lattice for Cr <sub>2</sub> O <sub>3</sub> (0001) .....	8
II. C. Construction of the reciprocal lattice vectors for the oxygen sub-lattice and the ( $\sqrt{3}\times\sqrt{3}$ )R30° structure of Cr <sub>2</sub> O <sub>3</sub> (0001) .....	9
II. D. Determination of Maxima Locations for Cr(110) and Cr <sub>2</sub> O <sub>3</sub> (0001) .....	10
<b>III. Experimental Approach</b> .....	<b>16</b>
III. A. The Sample Holder Assembly .....	17
III. B. The Electron Gun and Detector.....	18
<b>IV. Sample Preparation</b> .....	<b>20</b>
IV. A. Sputtering and Annealing .....	21
IV. B. Hot-sputtering .....	25
<b>V. Oxide Growth</b> .....	<b>27</b>
<b>VI. Analysis of Temperature Dependence</b> .....	<b>30</b>
<b>VII. Conclusions</b> .....	<b>33</b>

## List of Figures

Figure 1. (a) The (110) plane of a BCC conventional cell. The primitive (b) and reciprocal (c) lattice vectors. The real (d) and reciprocal (e) 2-D lattice for Cr(110) with the area of the primitive cell in grey.....	7
Figure 2. (a) The (0001) plane of a hexagonal conventional cell. The primitive (b) and reciprocal (c) lattice vectors. The real (d) Cr <sub>2</sub> O <sub>3</sub> (0001) surface showing the oxygen sub lattice and the reciprocal (e) 2-D lattice for Cr <sub>2</sub> O <sub>3</sub> (0001) with the primitive cell in grey. ....	8
Figure 3. The primitive (a) and reciprocal (c) lattice vectors for the $(\sqrt{3}\times\sqrt{3})R30^\circ$ conformation of the primitive cell of Cr <sub>2</sub> O <sub>3</sub> (0001). The primitive (b) and reciprocal (d) lattice vectors for the oxygen sub-lattice. (e) The real Cr <sub>2</sub> O <sub>3</sub> (0001) surface showing both the (1x1) and $(\sqrt{3}\times\sqrt{3})R30^\circ$ primitive cells. (f) The real oxygen sub-lattice with the primitive cell in grey and the Cr sites in outline.....	9
Figure 4. Geometric conventions for a beam of electrons incident upon a surface.....	10
Figure 5. The sample holder assembly .....	18
Figure 6. A schematic of an electron gun and detector assembly. a: filament. b: Wehnelt cylinder. c: anode. d: focusing lenses. e, f: grids 1 and 4, usually held at ground potential. g: phosphor screen, usually held at 3 to 5 kV. h: grids 2 and 3, held at slightly lower potential energy than incident beam energy. i: sample. ....	19
Figure 7. Mean free path of electrons in metallic solids as a function of their energy.....	20
Figure 8. LEED patterns of Cr(110) following twelve sputter/anneal cycles. Beam energies: 54.5eV (a), 75.1eV (b), 112.9eV (c), 164.6eV (d). ....	23
Figure 9. 54.5 eV LEED patterns of Cr(110) before (a) and after (b) hot-sputtering. Note: both images captured using identical shutter speeds. ....	25
Figure 10. LEED patterns of Cr(110) after hot-sputtering at 54.4 eV (a) and 75.1 eV (b). ....	26
Figure 11. LEED patterns obtained following the growth of a Cr <sub>2</sub> O <sub>3</sub> (0001) on Cr(110) at incident beam energies of 54.5eV (a), 75.1eV (b), 112.9eV (c), and 164.6eV (d).....	28
Figure 12. LEED patterns obtained following the growth of Cr <sub>2</sub> O <sub>3</sub> (0001) on Cr(110) at incident beam energies of 54.5eV (a) and 75.1eV (b). ....	29
Figure 13. LEED patterns obtained of Cr <sub>2</sub> O <sub>3</sub> (0001)/Cr(110) at 300K (a), 175K (b), 140K (c), and 675K (d). ....	31
Figure 14. LEED images reported by Bender <i>et al</i> at (a) 300 K and (c) 150 K. The diffraction patterns we obtained at (b) 300K and (d) 140 K. ....	32

## List of Tables

Table 1. The location of the first six diffraction maxima for Cr (110).....	14
Table 2. The location of the first twelve diffraction maxima for (1x1) Cr <sub>2</sub> O <sub>3</sub> (0001).....	14
Table 3. The location of the first twelve diffraction maxima for ( $\sqrt{3}\times\sqrt{3}$ )R30° Cr <sub>2</sub> O <sub>3</sub> (0001) .....	15
Table 4. The location of the first six diffraction maxima for the oxygen sub-lattice .....	15

## **Acknowledgements**

I have been very fortunate during the last two years to work in a dynamic research group under the mentoring eye of Dr. Carl Ventrice Jr. For his knowledge of condensed matter systems and the mechanics of experiment, and patience when dispensing either, I am sincerely grateful. Additionally, I would like to thank Nicolas Clark and Daniel Field, for writing the program to control the temperature of the crystal and for efforts in construction of our UHV chamber, respectively.

## Abstract

---

The (110) surface of Cr is somewhat unique in that its native oxide forms an epitaxial  $\text{Cr}_2\text{O}_3(0001)$  overlayer. Previous studies of this epitaxial surface found that a  $(\sqrt{3}\times\sqrt{3})R30^\circ$  surface reconstruction was observed over a temperature range of 125 K to 175 K, and this has been attributed to a surface magnetic transition. To determine the nature of this surface reconstruction, we have grown an epitaxial  $\text{Cr}_2\text{O}_3(0001)$  surface on a Cr(110) single crystal and characterized its surface structure over a temperature range of 140 K to 675 K using low energy electron diffraction (LEED). Before growth of the epitaxial oxide, the Cr(110) surface was cleaned by performing several cycles of sputtering the surface with Ar ions followed by annealing at 725 °C to heal the surface. Although moderate surface contamination was observed on the Cr(110) surface after several sputter/anneal cycles, it was possible to grow an epitaxial  $\text{Cr}_2\text{O}_3(0001)$  film, which exhibited the characteristic LEED pattern of the (1x1) structure at 300 K. Our film failed to exhibit the characteristic pattern of the  $(\sqrt{3}\times\sqrt{3})R30^\circ$  overlayer structure over the entire temperature range used in this study. It is possible that lingering impurities present in the bulk chromium prevented the reconstruction. However, it is noted that CO adsorption on this surface begins at 175 K and also results in a  $(\sqrt{3}\times\sqrt{3})R30^\circ$  overlayer. Since CO is present in all vacuum systems and itinerate magnetic effects are very unusual, the source of the surface reconstruction is most likely not from a surface magnetic transition but from CO adsorption at low temperatures. It is probable, due to the lower base pressure of our vacuum system in comparison to the previous studies, that the cleaner environment failed to provide sufficient CO to produce the  $(\sqrt{3}\times\sqrt{3})R30^\circ$  surface reconstruction during our measurement time.

---

## I. Introduction

Chromium ions can have multiple oxidation states. Therefore, chromium based transition metal oxides often exhibit a wide range of chemical properties at their surfaces. As a result, the oxidized surfaces of chromium are often used as catalysts and precursors in many chemical processes, such as hydrogenation and dehydrogenation of hydrocarbons<sup>1,2,3</sup>, replacement of chlorofluorocarbons<sup>4,5</sup>, and as passivation overlayers<sup>6,7</sup>. Additionally, oxidized chromium surfaces tend to exhibit novel magnetic and electronic traits due to electron interactions with the crystal potential<sup>8</sup>. These traits have great capability for utilization in detection of harmful gases<sup>9,10</sup>, magnetic recording devices<sup>11</sup>, and, more recently, spintronic devices<sup>12</sup>. For these applications, study of the growth processes and surface geometry of chromic oxides is of vital importance.

Large single crystals of Cr<sub>2</sub>O<sub>3</sub> are not commercially available. Subsequently, very few studies have been performed on bulk single crystals of Cr<sub>2</sub>O<sub>3</sub>. In addition, the characterization of Cr<sub>2</sub>O<sub>3</sub> by electron diffraction is difficult due to its semiconducting properties. During LEED, many of the incident electrons become trapped in chromium

---

<sup>1</sup> S. Derossi, G. Ferraris, S. Fremiotti, E. Garrone, G. Ghiotti, M. C. Campa and V. Indovina, *J. Catalysis* **148** 36 (1994).

<sup>2</sup> B. N. Lukyanov, *Russ. Chem. Rev.* **77** (11) 995 -1016 (2008)

<sup>3</sup> Kh. M. Minachev, Yu. S. Khodakov and V. S. Nakhshunov, *Russ. Chem. Rev.* **45** (2) 142 (1976)

<sup>4</sup> K. Neidersen, E. Schreier and E. Kemnitz, *J. Catalysis* **167** 210 (1997)

<sup>5</sup> A. Farrokhnia, B. Sakakini and K. C. Waugh, *J. Catalysis* **174** 219 (1998)

<sup>6</sup> J. B. Bult, W. G. Sawyer, P. M. Ajayan and L. S. Schadler, *Nanotechnology* **20** 1 (2009)

<sup>7</sup> C. A. Ventrice Jr and H. Geisler, in *Thin Films: Heteroepitaxial Systems*, edited by W. K. Lui and M. B. Santos (World Scientific, Singapore, 1999) Vol. 15, p. 195.

<sup>8</sup> D. N. Astrov, *Sov. Phys.—JETP* **13** 729 (1961)

<sup>9</sup> D. Jing, W. Yiquan and C. Kwang-Leong, *Thin Solid Films* **497** 42 (2006)

<sup>10</sup> G. A. Shaw, I. P. Parkin and D. E. Williams, *J. Mater. Chem.* **13** 2957 (2003)

<sup>11</sup> S. A. Makhlof, *J. Magn. Mater.* **272** 1530 (2004)

<sup>12</sup> A. F. Mota, A. J. Silvestre, P. M. Sousa, O. Conde, M. A. Rosa and M. Godinho, *Mater. Sci. Forum* **289** 514 (2006)

oxide, building up a charge in the crystal, due to the band gap ( $\Delta E = 3.2 \text{ eV}$ )<sup>13</sup>. To avoid this sample-charging effect, thin films of chromic oxide are commonly grown heteroepitaxially on bulk single crystal chromium. Several groups have successfully produced this heteroepitaxial native oxide surface through vapor phase and molecular beam growth techniques and characterized the  $\text{Cr}_2\text{O}_3(0001)/\text{Cr}(110)$  thin film surface<sup>14,15</sup>. While studies of thin film systems elucidate many of the properties potentially exhibited in the bulk, a clear picture of the surfaces of  $\text{Cr}_2\text{O}_3$  is occluded by substrate-adsorbate interactions, which may cause deviations from the ideal bulk termination.

Previous investigation of the surface region of  $\text{Cr}_2\text{O}_3(0001)$  has uncovered evidence through low energy electron diffraction and electron energy loss spectroscopy analysis to support an antiferromagnetic coupling of the first two chromium layers when cooled to low temperatures<sup>16,17</sup>. This coupling is believed to be the source of a surface reconstruction evidenced by the emergence of a  $(\sqrt{3}\times\sqrt{3})R30^\circ$  LEED pattern, which exhibits a maximum intensity at 150K. To experimentally verify these findings, we have grown  $\text{Cr}_2\text{O}_3(0001)$  heteroepitaxially on  $\text{Cr}(110)$  in ultra high vacuum by vapor phase methods and characterized the surface using LEED analysis while varying the temperature of the crystal through the range defined in the previous work.

---

<sup>13</sup> D.S. McClure, J. Chem. Phys. **38**, 2289 (1963)

<sup>14</sup> H. -J. Freund, B. Dillmann, O. Seiferth, G. Klivenyi, M. Bender, D. Ehrlich, I. Hemmerich and D. Cappus, Catalysis Today, **32** 1 (1996)

<sup>15</sup> A. Stierle and H. Zabel, Europhys. Lett. **37** 365 (1997)

<sup>16</sup> T. Takano, M. Wilde, M. Matsumoto, T. Okano, and K. Fukutani, e-J. Surf. Sci. Nanotech. **4** 534 (2006)

<sup>17</sup> M. Bender, D. Ehrlich, I. N. Yadovkin, F. Rohr, M. Bäumer, H. Kuhlenbeck, H.-J. Freund, and V. Staemmler, J. Phys.:Condens. Matter **7**, 5289 (1995)

## II. Theoretical Approach

In crystalline solids, all of the atoms are arranged periodically in a structure called a lattice. Each crystal's lattice is defined in real space by three primitive basis vectors ( $\mathbf{x}_1, \mathbf{x}_2, \mathbf{x}_3$ ). The translational symmetry of the lattice is apparent in that any point in the lattice can be obtained through an integer sum of these primitive vectors.

$$\mathbf{r} = m_1\mathbf{x}_1 + m_2\mathbf{x}_2 + m_3\mathbf{x}_3 \quad (1)$$

The three primitive basis vectors form a three-dimensional structure called the primitive unit cell. The primitive unit cell is defined as the smallest structure that displays the periodicity of the lattice and contains only one lattice point<sup>18</sup>. Even though there may be more than one configuration of the primitive cell, each construction is equivalent.

It is of fundamental importance in diffraction studies to understand the interactions of electrons when encountering a potential field created by a periodic arrangement of atoms. When a beam of electrons is fired at the surface of a crystalline solid, there are two possible events for any specific electron in the beam to experience. First, it may be scattered by the strong potentials inside of the crystal, either forward, into the crystal, or backward out of the crystal. Second, it can undergo a loss of energy. We are concerned with only the elastic back-scattering events because of the configuration of our experimental apparatus, which will be described later. Because the probability of locating backscattered electrons is spatially variant, there is a higher probability of

---

<sup>18</sup> M. A. Omar, *Elementary Solid State Physics* (Addison-Wesley, Reading, 1975) p. 5.

finding an electron in certain regions of space due to the constructive interference of multiple wavefunctions.

To understand the process of this interference, we begin by considering an electron in the periodic potential of a crystal lattice. An electron in this potential has a Hamiltonian in the form of equation 2<sup>19</sup>.

$$H = -\frac{\hbar^2}{2m}\nabla^2 + V(\mathbf{r}) \quad (2)$$

By virtue of Bloch's Theorem<sup>20</sup>, we can consider the eigenfunctions of this Hamiltonian to be the product of the wavefunction of a plane wave and a function that exhibits the periodicity of the potential.

$$\varphi(\mathbf{r}) = u(\mathbf{r})e^{i\mathbf{k}\cdot\mathbf{r}} \quad (3)$$

This is not to say that  $\varphi(\mathbf{r})$  has the periodicity of the crystal. However, we can uncover the wavefunction's periodicity by examining  $u(\mathbf{r})$ . Because the potential acting on incident electrons is due to the electrons of the crystal, the potential must be equivalent when translated to any corresponding site within the crystal.

$$V(\mathbf{r}) = V(\mathbf{r} + a\mathbf{x}_1 + b\mathbf{x}_2 + c\mathbf{x}_3) \quad (4)$$

Then  $u(\mathbf{r})$  exhibits the same translational symmetry.

$$u(\mathbf{r}) = u(\mathbf{r} + a\mathbf{x}_1 + b\mathbf{x}_2 + c\mathbf{x}_3) \quad (5)$$

---

<sup>19</sup> R. L. Liboff, *Introductory Quantum Mechanics* (Addison-Wesley, San Francisco, 2003) p 291.

<sup>20</sup> Bloch, F. Z. Physik **52** 555 (1928).

We can then write  $u(\mathbf{r})$  as an exponential Fourier series.

$$u(\mathbf{r}) = \sum_{\mathbf{g}} c_{\mathbf{g}} e^{i(\mathbf{g} \cdot \mathbf{r})} \quad (6)$$

Then by virtue of equation (5), we have the following equality

$$\begin{aligned} \sum_{\mathbf{g}} c_{\mathbf{g}} e^{i(\mathbf{g} \cdot \mathbf{r})} &= \sum_{\mathbf{g}} c_{\mathbf{g}} e^{i(\mathbf{g} \cdot (\mathbf{r} + a\mathbf{x}_1 + b\mathbf{x}_2 + c\mathbf{x}_3))} \\ 1 &= e^{i(\mathbf{g} \cdot a\mathbf{x}_1)} e^{i(\mathbf{g} \cdot b\mathbf{x}_2)} e^{i(\mathbf{g} \cdot c\mathbf{x}_3)} \end{aligned} \quad (7)$$

The values allowed for the summation variable  $\mathbf{g}$  by equation (7) are those that satisfy the Laue equations<sup>21</sup>.

$$\begin{aligned} \mathbf{g} \cdot \mathbf{x}_1 &= \text{integer} \times 2\pi \\ \mathbf{g} \cdot \mathbf{x}_2 &= \text{integer} \times 2\pi \\ \mathbf{g} \cdot \mathbf{x}_3 &= \text{integer} \times 2\pi \end{aligned} \quad (8)$$

Combining this result with (3) yields

$$\varphi(\mathbf{r}) = \sum_{\mathbf{g}} c_{\mathbf{g}} e^{i[(\mathbf{g} + \mathbf{k}) \cdot \mathbf{r}]} \quad (9)$$

Therefore, the scattered wavefunction demonstrates the translational symmetry of this Fourier expansion. The expansion variable  $\mathbf{g}$  can be dissolved into separate components, which comprise an orthogonal basis that is orthonormal to the real basis. This creates a new set of vectors,  $\mathbf{g}(\mathbf{x}_1^*, \mathbf{x}_2^*, \mathbf{x}_3^*)$ , and a new lattice, which is called the reciprocal lattice.

---

<sup>21</sup> C. Kittel, *Introduction to Solid State Physics*, (Wiley, New York, 1996) 7<sup>th</sup> ed., p.

$$\mathbf{g} = n_1 \mathbf{x}_1^* + n_2 \mathbf{x}_2^* + n_3 \mathbf{x}_3^* \quad (10)$$

The construction of the reciprocal lattice from its corresponding real lattice can be performed with the following equations where  $\Omega_c$  is the volume of a primitive cell<sup>17</sup>.

$$\begin{aligned} \mathbf{x}_1^* &= \frac{2\pi}{\Omega_c} (\mathbf{x}_2 \times \mathbf{x}_3) \\ \mathbf{x}_2^* &= \frac{2\pi}{\Omega_c} (\mathbf{x}_3 \times \mathbf{x}_1) \\ \mathbf{x}_3^* &= \frac{2\pi}{\Omega_c} (\mathbf{x}_1 \times \mathbf{x}_2) \end{aligned} \quad (11)$$

The reciprocal lattice may only be constructed from vectors that form a primitive cell in the real lattice. Understanding the relationship between the real and reciprocal lattices is therefore tantamount to translating the LEED pattern into a surface structure.

## II. A. Construction of the Reciprocal Lattice for Chromium(110)

Chromium crystallizes in the body-centered cubic (BCC) structure<sup>22</sup> with a conventional cell lattice constant  $a_0$  of  $2.88 \text{ \AA}$ <sup>21</sup>. The (110) plane of this structure forms a quasi-hexagonal periodic surface (figure 1.a), which is evidenced by the internal angle  $\theta = 70.5^\circ$  (figure 1.b).

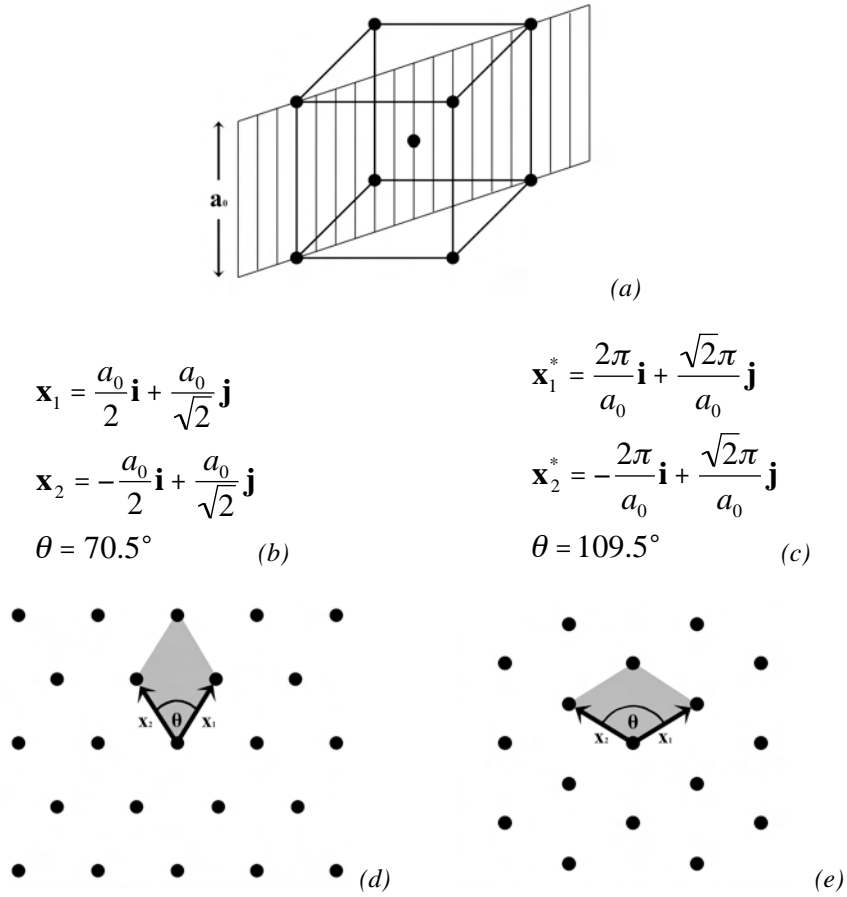


Figure 1. (a) The (110) plane of a BCC conventional cell. The primitive (b) and reciprocal (c) lattice vectors. The real (d) and reciprocal (e) 2-D lattice for Cr(110) with the area of the primitive cell in grey.

<sup>22</sup> A. W. Hull, Phys. Rev. **17**, 571, (1921).

## II. B. Construction of the Reciprocal Lattice for $\text{Cr}_2\text{O}_3(0001)$

Chromium sesquioxide crystallizes in the corundum structure<sup>23</sup>, which exhibits a hexagonal conventional cell (figure 2.a). The structure consists of a hexagonally close packed oxygen sub-lattice with chromium atoms occupying two thirds of the octahedral sites (figure 2.d). The lattice parameters of this structure are  $a_0 = 4.95 \text{ \AA}$ , and  $c_0 = 13.58 \text{ \AA}$ .

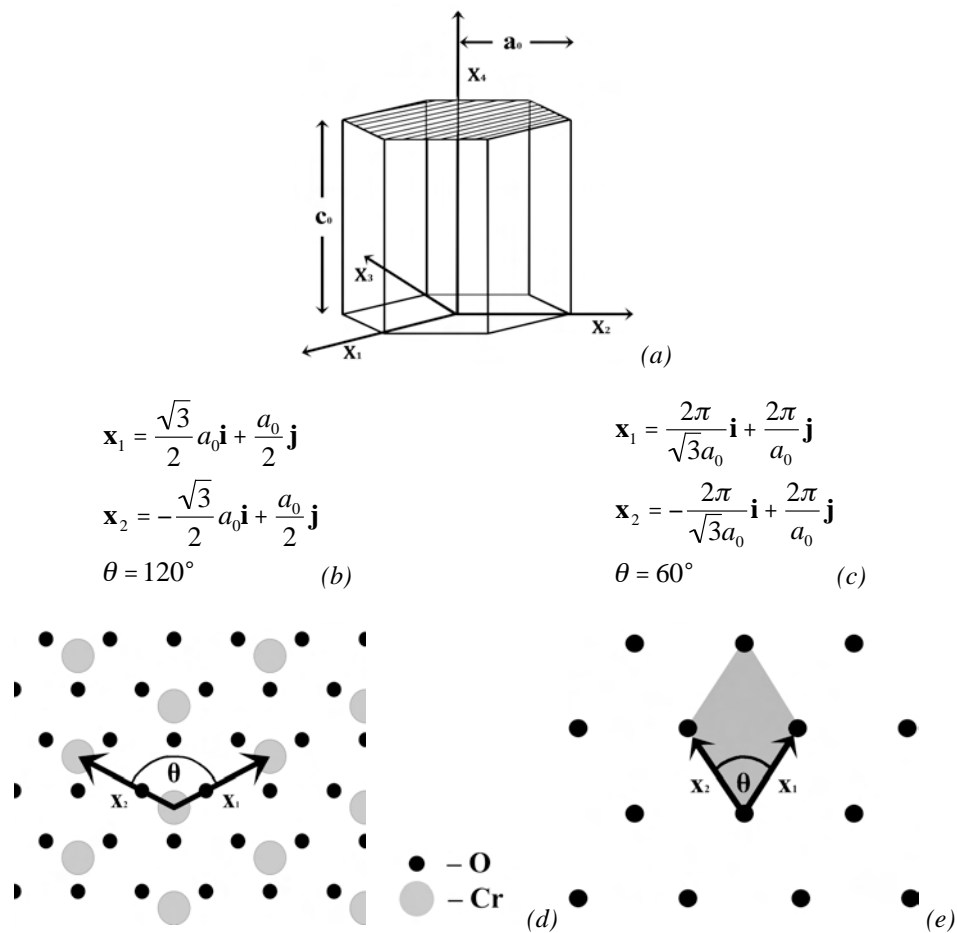


Figure 2. (a) The (0001) plane of a hexagonal conventional cell. The primitive (b) and reciprocal (c) lattice vectors. The real (d)  $\text{Cr}_2\text{O}_3(0001)$  surface showing the oxygen sub lattice and the reciprocal (e) 2-D lattice for  $\text{Cr}_2\text{O}_3(0001)$  with the primitive cell in grey.

<sup>23</sup> Wyckoff, R.W.G., *Crystal Structures*, (Interscience, New York, 1969) 2<sup>nd</sup> ed.

II. C. Construction of the reciprocal lattice vectors for the oxygen sub-lattice and the  $(\sqrt{3} \times \sqrt{3})R30^\circ$  structure of  $\text{Cr}_2\text{O}_3(0001)$

The  $(\sqrt{3} \times \sqrt{3})R30^\circ$  structure is found by multiplying each of the primitive lattice vectors by  $\sqrt{3}$  and rotating each vector  $30^\circ$  in the positive  $\varphi$ -direction (figure 3.e). The relationship between the chromium lattice and the oxygen sub-lattice is that the chromium is positioned in the  $(\sqrt{3} \times \sqrt{3})R30^\circ$  sites of the oxygen sub-lattice (figure 3.f).

$$\begin{aligned} \mathbf{x}_1 &= \frac{3}{2}a_0\mathbf{i} + \frac{\sqrt{3}}{2}a_0\mathbf{j} \\ \mathbf{x}_2 &= -\frac{3}{2}a_0\mathbf{i} + \frac{\sqrt{3}}{2}a_0\mathbf{j} \\ \theta &= 120^\circ \end{aligned} \quad (a)$$

$$\begin{aligned} \mathbf{x}_1 &= \frac{\sqrt{3}}{6}a_0\mathbf{i} + \frac{a_0}{2}\mathbf{j} \\ \mathbf{x}_2 &= -\frac{\sqrt{3}}{6}a_0\mathbf{i} + \frac{a_0}{2}\mathbf{j} \\ \theta &= 60^\circ \end{aligned} \quad (b)$$

$$\begin{aligned} \mathbf{x}_1^* &= \frac{2\pi}{3a_0}\mathbf{i} + \frac{2\pi}{\sqrt{3}a_0}\mathbf{j} \\ \mathbf{x}_2^* &= -\frac{2\pi}{3a_0}\mathbf{i} + \frac{2\pi}{\sqrt{3}a_0}\mathbf{j} \\ \theta &= 60^\circ \end{aligned} \quad (c)$$

$$\begin{aligned} \mathbf{x}_1^* &= \frac{\sqrt{12}\pi}{a_0}\mathbf{i} + \frac{2\pi}{a_0}\mathbf{j} \\ \mathbf{x}_2^* &= -\frac{\sqrt{12}\pi}{a_0}\mathbf{i} + \frac{2\pi}{a_0}\mathbf{j} \\ \theta &= 120^\circ \end{aligned} \quad (d)$$

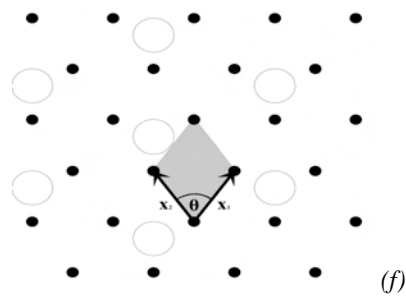
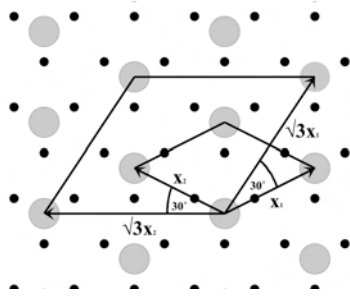


Figure 3. The primitive (a) and reciprocal (c) lattice vectors for the  $(\sqrt{3} \times \sqrt{3})R30^\circ$  conformation of the primitive cell of  $\text{Cr}_2\text{O}_3(0001)$ . The primitive (b) and reciprocal (d) lattice vectors for the oxygen sub-lattice. (e) The real  $\text{Cr}_2\text{O}_3(0001)$  surface showing both the  $(1 \times 1)$  and  $(\sqrt{3} \times \sqrt{3})R30^\circ$  primitive cells. (f) The real oxygen sub-lattice with the primitive cell in grey and the Cr sites in outline.

#### II. D. Determination of Maxima Locations for Cr(110) and Cr<sub>2</sub>O<sub>3</sub>(0001)

For electron diffraction, we are concerned with the elastically scattered electrons because they produce the entire diffraction pattern. To locate the diffraction maxima, we can utilize conservation of momentum. The difference between the incident and reflected electron beam momentum defines a scattering vector,  $\Delta\mathbf{k}$ . The typical conventions used are shown in figure 4.

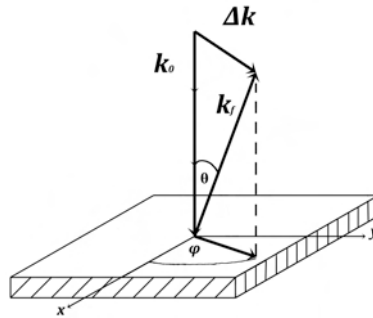


Figure 4. Geometric conventions for a beam of electrons incident upon a surface.

The Laue conditions (8) allow for constructive interference only when the scattering vector is equal to a reciprocal lattice vector.

$$\Delta\mathbf{k} = \mathbf{g} \quad (12)$$

Because electrons do not travel more than a few monolayers into a surface, the component of momentum perpendicular to the surface can be disregarded in the calculation of the position of diffraction maxima. The parallel component of momentum is given by equation (13).

$$\Delta\mathbf{k}_{\parallel} = k \sin\theta \cos\phi \mathbf{i} + k \sin\theta \sin\phi \mathbf{j} \quad (13)$$

By inserting the reciprocal lattice vectors (figure 1.c) for chromium into (12), we find:

$$k \sin \theta \cos \phi \mathbf{i} + k \sin \theta \sin \phi \mathbf{j} = \frac{2\pi}{a_0} (n_1 - n_2) \mathbf{i} + \frac{\sqrt{2}\pi}{a_0} (n_1 + n_2) \mathbf{j} \quad (14)$$

Likewise, insertion of the reciprocal lattice vectors for  $\text{Cr}_2\text{O}_3$  (figure 2.c), the  $(\sqrt{3} \times \sqrt{3})R30^\circ$  structure of  $\text{Cr}_2\text{O}_3$  (figure 3.c), and the oxygen sub-lattice (figure 3.d) respectively yields:

$$k \sin \theta \cos \phi \mathbf{i} + k \sin \theta \sin \phi \mathbf{j} = \frac{2\pi}{\sqrt{3}a_0} (n_1 - n_2) \mathbf{i} + \frac{2\pi}{a_0} (n_1 + n_2) \mathbf{j} \quad (15)$$

$$k \sin \theta \cos \phi \mathbf{i} + k \sin \theta \sin \phi \mathbf{j} = \frac{2\pi}{3a_0} (n_1 - n_2) \mathbf{i} + \frac{2\pi}{\sqrt{3}a_0} (n_1 + n_2) \mathbf{j} \quad (16)$$

$$k \sin \theta \cos \phi \mathbf{i} + k \sin \theta \sin \phi \mathbf{j} = \frac{\sqrt{12}\pi}{a_0} (n_1 - n_2) \mathbf{i} + \frac{2\pi}{a_0} (n_1 + n_2) \mathbf{j} \quad (17)$$

Then we can equate the magnitudes of these equations.

$$\begin{aligned} |\Delta \mathbf{k}_\parallel| &= |\mathbf{g}_\parallel| \\ \Delta \mathbf{k}_\parallel \cdot \Delta \mathbf{k}_\parallel &= \mathbf{g}_\parallel \cdot \mathbf{g}_\parallel \end{aligned} \quad (18)$$

Employing (18) on Cr(110), equation (14), yields:

$$\begin{aligned} k^2 \sin^2 \theta \cos^2 \phi + k^2 \sin^2 \theta \sin^2 \phi &= \frac{4\pi^2}{a_0^2} (n_1 - n_2)^2 + \frac{2\pi^2}{a_0^2} (n_1 + n_2)^2 \\ k^2 \sin^2 \theta &= \frac{4\pi^2}{a_0^2} \left[ (n_1 - n_2)^2 + \frac{1}{2} (n_1 + n_2)^2 \right] \end{aligned} \quad (19)$$

Additionally for (1x1)Cr<sub>2</sub>O<sub>3</sub>(0001), ( $\sqrt{3}\times\sqrt{3}$ )R30° Cr<sub>2</sub>O<sub>3</sub>(0001), and the oxygen sub-lattice, equations (15), (16), and (17) respectively, we have:

$$k^2 \sin^2 \theta = \frac{4\pi^2}{a_0^2} \left[ \frac{1}{3} (n_1 - n_2)^2 + (n_1 + n_2)^2 \right] \quad (20)$$

$$k^2 \sin^2 \theta = \frac{4\pi^2}{3a_0^2} \left[ \frac{1}{3} (n_1 - n_2)^2 + (n_1 + n_2)^2 \right] \quad (21)$$

$$k^2 \sin^2 \theta = \frac{12\pi^2}{a_0^2} \left[ (n_1 - n_2)^2 + \frac{1}{3} (n_1 + n_2)^2 \right] \quad (22)$$

Using the energy of a plane wave and substituting in the de Broglie wavelength we obtain an expression for the energy that is dependent on wave number.

$$E = \frac{p^2}{2m_e} = \frac{h^2}{2m_e \lambda^2} = \frac{\hbar^2 k^2}{2m_e} \quad (23)$$

Inserting (23) into (19), (20), (21), and (22), we can solve for  $\theta$ .

$$\theta = \sin^{-1} \left[ \frac{2\pi^2 \hbar^2}{m_e a_0^2 E} \left[ (n_1 - n_2)^2 + \frac{1}{2} (n_1 + n_2)^2 \right] \right]^{1/2} \quad (24)$$

$$\theta = \sin^{-1} \left[ \frac{2\pi^2 \hbar^2}{m_e a_0^2 E} \left[ \frac{1}{3} (n_1 - n_2)^2 + (n_1 + n_2)^2 \right] \right]^{1/2} \quad (25)$$

$$\theta = \sin^{-1} \left[ \frac{2\pi^2 \hbar^2}{3m_e a_0^2 E} \left[ \frac{1}{3} (n_1 - n_2)^2 + (n_1 + n_2)^2 \right] \right]^{1/2} \quad (26)$$

$$\theta = \sin^{-1} \left[ \frac{6\pi^2 \hbar^2}{m_e a_0^2 E} \left[ (n_1 - n_2)^2 + \frac{1}{3} (n_1 + n_2)^2 \right] \right]^{1/2} \quad (27)$$

Once we have discerned  $\theta$  for a given energy, we can equate the colinear vector portions from the right- and left-hand sides of equation (14) to solve for  $\phi$ .

$$\begin{aligned}\phi &= \cos^{-1} \left[ \frac{2\pi\hbar}{\sqrt{2m_e a_0^2 E}} \frac{1}{\sin\theta} (n_1 - n_2) \right] \\ \phi &= \sin^{-1} \left[ \frac{\pi\hbar}{\sqrt{m_e a_0^2 E}} \frac{1}{\sin\theta} (n_1 + n_2) \right]\end{aligned}\quad (28)$$

Performing the same vector analysis on equations (15), (16), and (17) yields:

$$\begin{aligned}\phi &= \cos^{-1} \left[ \frac{2\pi\hbar}{\sqrt{6m_e a_0^2 E}} \frac{1}{\sin\theta} (n_1 - n_2) \right] \\ \phi &= \sin^{-1} \left[ \frac{2\pi\hbar}{\sqrt{2m_e a_0^2 E}} \frac{1}{\sin\theta} (n_1 + n_2) \right]\end{aligned}\quad (29)$$

$$\begin{aligned}\phi + 30^\circ &= \cos^{-1} \left[ \frac{2\pi\hbar}{3\sqrt{2m_e a_0^2 E}} \frac{1}{\sin\theta} (n_1 - n_2) \right] \\ \phi + 30^\circ &= \sin^{-1} \left[ \frac{2\pi\hbar}{\sqrt{6m_e a_0^2 E}} \frac{1}{\sin\theta} (n_1 + n_2) \right]\end{aligned}\quad (30)$$

$$\begin{aligned}\phi &= \cos^{-1} \left[ \frac{\sqrt{6}\pi\hbar}{\sqrt{m_e a_0^2 E}} \frac{1}{\sin\theta} (n_1 - n_2) \right] \\ \phi &= \sin^{-1} \left[ \frac{2\pi\hbar}{\sqrt{2m_e a_0^2 E}} \frac{1}{\sin\theta} (n_1 + n_2) \right]\end{aligned}\quad (31)$$

Note: So that the relative axes are equivalent for the calculation of  $\phi$  for the (1x1) and  $(\sqrt{3}\times\sqrt{3})R30^\circ$  structures of  $\text{Cr}_2\text{O}_3(0001)$ , an additional phase angle of  $30^\circ$  degree was inserted into (30). The results of these equations are collected in tables 1,2,3 and 4.

Table 1. The location of the first six diffraction maxima for Cr (110)

Beam Energy (eV)	$(h,k)$	$\theta$ (deg)	$\phi$ (deg)	Beam Energy (eV)	$(h,k)$	$\theta$ (deg)	$\phi$ (deg)
54.5	$(0,1)$	45	144.76	75.1	$(0,1)$	37	144.76
	$(1,0)$	45	35.26		$(1,0)$	37	35.26
	$(-1,0)$	45	215.26		$(-1,0)$	37	215.26
	$(0,-1)$	45	324.76		$(0,-1)$	37	324.76
	$(1,-1)$	54.74	90		$(1,1)$	44.02	90
	$(-1,1)$	54.74	270		$(-1,-1)$	44.02	270

Table 2. The location of the first twelve diffraction maxima for  $(1 \times 1)$   $\text{Cr}_2\text{O}_3$  (0001)

Beam Energy (eV)	$(h,k)$	$\theta$ (deg)	$\phi$ (deg)	Beam Energy (eV)	$(h,k)$	$\theta$ (deg)	$\phi$ (deg)
54.5	$(0,1)$	22.8	120	75.1	$(0,1)$	19.28	120
	$(1,0)$	22.8	60		$(1,0)$	19.28	60
	$(-1,0)$	22.8	300		$(-1,0)$	19.28	300
	$(0,-1)$	22.8	240		$(0,-1)$	19.28	240
	$(-1,1)$	22.8	180		$(-1,1)$	19.28	180
	$(1,-1)$	22.8	0		$(1,-1)$	19.28	0
	$(1,1)$	42.16	90		$(1,1)$	34.88	90
	$(-1,-1)$	42.16	270		$(-1,-1)$	34.88	270
	$(2,-1)$	42.16	30		$(2,-1)$	34.88	30
	$(-2,1)$	42.16	210		$(-2,1)$	34.88	210
	$(1,-2)$	42.16	330		$(1,-2)$	34.88	330
	$(-1,2)$	42.16	150		$(-1,2)$	34.88	150

Table 3. The location of the first twelve diffraction maxima for  $(\sqrt{3}\times\sqrt{3})R30^\circ$   $\text{Cr}_2\text{O}_3$  (0001)

Beam Energy (eV)	$(h,k)$	$\theta$ (deg)	$\phi$ (deg)	Beam Energy (eV)	$(h,k)$	$\theta$ (deg)	$\phi$ (deg)
54.5	$(0,1)$	12.94	90	75.1	$(0,1)$	11	90
	$(1,0)$	12.94	30		$(1,0)$	11	30
	$(-1,0)$	12.94	270		$(-1,0)$	11	270
	$(0,-1)$	12.94	210		$(0,-1)$	11	210
	$(-1,1)$	12.94	150		$(-1,1)$	11	150
	$(1,-1)$	12.94	330		$(1,-1)$	11	330
	$(1,1)$	22.83	60		$(1,1)$	19.28	60
	$(-1,-1)$	22.83	240		$(-1,-1)$	19.28	240
	$(2,-1)$	22.83	0		$(2,-1)$	19.28	0
	$(-2,1)$	22.83	180		$(-2,1)$	19.28	180
	$(1,-2)$	22.83	300		$(1,-2)$	19.28	300
	$(-1,2)$	22.83	120		$(-1,2)$	19.28	120

Table 4. The location of the first six diffraction maxima for the oxygen sub-lattice

Beam Energy (eV)	$(h,k)$	$\theta$ (deg)	$\phi$ (deg)	Beam Energy (eV)	$(h,k)$	$\theta$ (deg)	$\phi$ (deg)
54.5	$(0,1)$	42.20	150	75.1	$(0,1)$	34.88	150
	$(1,0)$	42.20	30		$(1,0)$	34.88	30
	$(-1,0)$	42.20	210		$(-1,0)$	34.88	210
	$(0,-1)$	42.20	330		$(0,-1)$	34.88	330
	$(1,1)$	42.20	90		$(1,1)$	34.88	90
	$(-1,-1)$	42.20	270		$(-1,-1)$	34.88	270

### III. Experimental Approach

The use of low energy electrons for studying the crystal structure of surfaces has a long history. The first experimental confirmation of the wave-like nature of electrons was performed in 1927 by Davisson and Germer. In their experiment, electrons were scattered from a nickel crystal in high vacuum<sup>24</sup>. Davisson and Germer were fortunate in that nickel is also one of the few materials that develop an ordered native oxide. Subsequent surface characterizations of other materials floundered on the basis that the oxide layers that develop on their surfaces do not exhibit high enough order to yield diffraction patterns. Crystallographers then turned to high energy electrons for their ability to tunnel farther into materials to regions of higher order.

Low energy electron diffraction reemerged as a tool in surface studies following the development of ultra high vacuum (UHV) in the 1960's<sup>25</sup>. This revival was driven by both the development of new, more powerful pumping devices and sputtering and annealing, which facilitated the preparation of atomically clean surfaces. The surface region of a material becomes quickly contaminated when exposed to atmospheric conditions. For example, at a pressure of  $\sim 10^{-6}$  Torr, the quantity of residual gases in the vacuum chamber impinging on the surface of the crystal provide the conditions necessary to potentially create a monolayer of impurities every second<sup>26</sup>. By employing modern UHV technology, the internal pressure of experimental chambers commonly falls below  $\sim 10^{-10}$  Torr. Pressures on this order increase the time necessary to potentially form a

---

<sup>24</sup> C. Davisson and L. H. Germer, *Nature* **119**, 558 (1927)

<sup>25</sup> J. B. Pendry, *Low Energy Electron Diffraction*, (Academic Press, London, 1974) p. 2.

<sup>26</sup> A. U. MacRae, *Science* **139** (3553), 379 (1963)

monolayer of surface contamination to more than two hours, which is sufficient time to perform a surface analysis.

The experimental apparatus that allows us to perform low energy electron diffraction consists of four major components: a UHV chamber, a sample holder that is capable of moving and controlling the temperature of the sample, an electron gun, and a detection mechanism for the scattered electrons. The UHV chamber used in this experiment maintains a base pressure of  $4 \times 10^{-11}$  Torr.

### III. A. The Sample Holder Assembly

The sample holder assembly (shown in figure 6) was constructed out of oxygen free high conductivity (OFHC) copper, and is connected to the chamber via an x-y-z manipulator with a differentially pumped rotary motion feed-through. The holder assembly is mounted at the end of a Dewar, which can be filled with liquid nitrogen ( $\text{LN}_2$ ) that is used to cool the sample to  $\sim 140$  K. Compressed air can also be blown into the Dewar to prevent the holder assembly from overheating during annealing of the sample. The sample was attached to a molybdenum insert by spot-welding two .005" tantalum wires to the edges of the crystal and the insert. The insert is held into the copper holder assembly by two molybdenum leaf springs. Additionally, a type K (chromel-alumel) thermocouple was spot-welded to the edge of the crystal to monitor the temperature during the measurements. Heating of the sample is achieved either by radiative heating from a filament mounted behind the sample or by electron-beam heating from the filament by biasing the sample at +750 V.

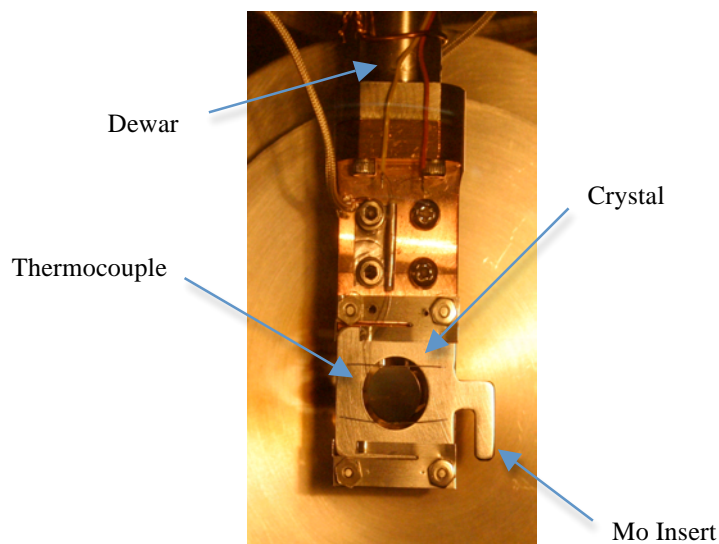


Figure 5. The sample holder assembly

### III. B. The Electron Gun and Detector

The beam of electrons, to be directed at the sample, is created inside of an electron gun by thermionic emission from a filament. The electrons are extracted from the filament by a Wehnelt cylinder. Then the electron beam passes through a series of anodes with the purpose of creating a well-collimated beam. The end of the electron gun is usually held at ground, as is the crystal, so that emergent electrons are only deflected from their line of flight by stray magnetic fields. After the incident electrons interact with the surface of the crystal, the back-scattered electrons pass through a series of hemispherical grids before they are collected at a hemispherical phosphor screen. The first grid is held at ground to ensure the region between the sample and detector is free of electric fields. The second and third grids act as gates that block the transmission of inelastically scattered electrons, which is why we are able to focus our theoretical discussion upon elastically scattered electrons. To accomplish this, second and third

grids are held at a potential energy, which is slightly less than the electron beam energy. The fourth grid is also held at ground, while the phosphor screen is raised to a potential of  $\sim 3000\text{V}$ , which accelerates elastically scattered electrons toward the screen with sufficient energy to produce phosphorescence. The configuration of the electron gun and detector is shown in figure 7.

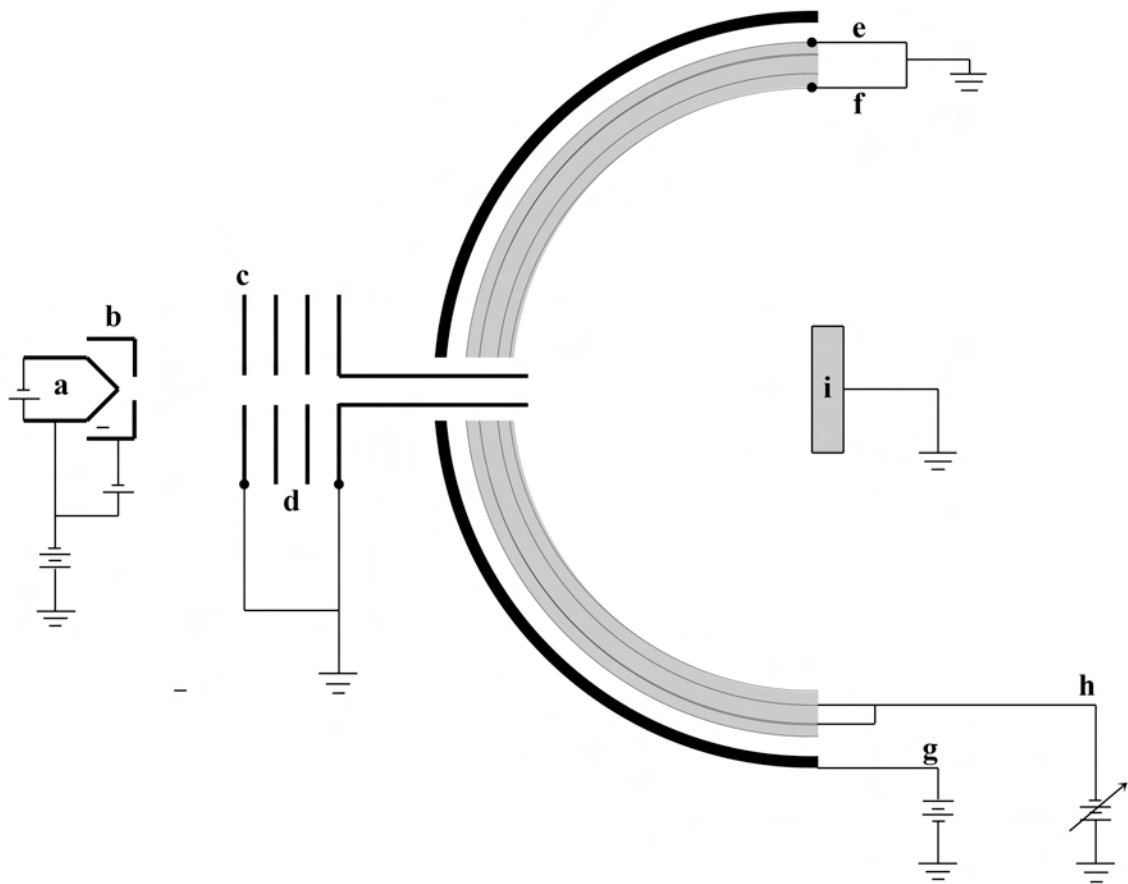


Figure 6. A schematic of an electron gun and detector assembly. a: filament. b: Wehnelt cylinder. c: anode. d: focusing lenses. e, f: grids 1 and 4, usually held at ground potential. g: phosphor screen, usually held at 3 to 5 kV. h: grids 2 and 3, held at slightly lower potential energy than incident beam energy. i: sample.

## IV. Sample Preparation

The average distance an electron can travel in matter before the magnitude of the momentum is no longer conserved in a scattering event is called the inelastic mean free path. Because our apparatus is sensitive only to elastically scattered electrons (those whose momentum is conserved), the mean free path is synonymous with the depth of the surface region under scrutiny. In most metals, the inelastic mean free path depends predominantly on the energy of the incident electrons and not the chemical identity of the solid; therefore, the mean free path, as a function of energy, falls on a universal curve (shown in figure 7). Consequently, at energies common to low energy electron diffraction studies (25 – 400 eV), back-scattered electrons are only collected from atoms in the first three to four atomic layers. Thus, the establishment of an atomically clean surface is essential to achieving clear and tractable diffraction patterns.

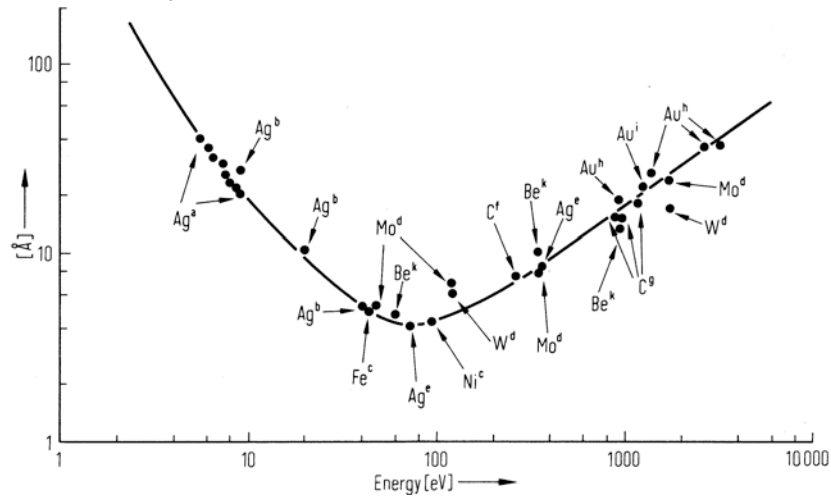


Figure 7. Mean free path of electrons in metallic solids as a function of their energy<sup>27</sup>

---

<sup>27</sup> G. Ertl and J. Küppers, *Low Energy Electrons and Surface Chemistry*, (Verlag Chemie, Weinheim, 1974) p. 7.

The chromium single crystal used in this experiment was purchased from Princeton Scientific Corp. The crystal is a disk 10 mm in diameter and 2 mm wide, with a flat machined along the [100] direction for orientation purposes. The crystal surface is polished to within  $\pm 0.1^\circ$  of the [110] direction. To remove contaminants such as fingerprints or polishing solvents, the crystal was cleaned ultrasonically first in acetone and then in methanol prior to mounting the crystal inside the UHV chamber. Once the crystal was under vacuum, the sample was repeatedly bombarded with noble gas ions, and flashed to high temperature to remove impurities and defects. The chamber pressure was monitored throughout the sample preparation process by an ion gauge.

#### IV. A. Sputtering and Annealing

The bombardment of the crystal with noble gas ions is referred to as ion sputtering and was developed in the 1950s<sup>28</sup>. In this technique, the vacuum chamber is backfilled with the inert gas to the desired pressure through a variable leak valve. The gas atoms are then ionized in an ion gun by electron impact ionization. Subsequently, the ions are accelerated through a potential and focused toward the crystal. This process is successful in removing impurities through collisions with surface structures and through the transfer of sufficient energy from incident ions to desorb surface atoms into vacuum. The scouring effect of ion sputtering, while effective in removing surface atoms, disorders the surface region of the sample. Therefore, another process is needed to heal the crystal. To allow substrate atoms adequate mobility to re-order, the temperature of the entire crystal must be raised to a relatively high temperature, typically 500 °C or

---

<sup>28</sup> H. E. Farnsworth, R. E. Schlier, T. H. George and R. M. Burger, *J. Appl. Phys.*, **29**, 1150 (1958); *J. Appl. Phys.*, **26**, 252 (1955)

higher for most metals. This is accomplished by radiant heating from a hot filament and/or by electron beam excitation. Although annealing does allow the surface to re-order, the high temperatures also permit contaminants within the bulk to segregate to the surface. Because of this ancillary effect, several sputter/anneal cycles are necessary to achieve a clean, well-ordered surface satisfactory for LEED analysis.

In this experiment, the chamber was backfilled with argon to a pressure of  $5 \times 10^5$  Torr. In the first four sputter cycles, the ions were accelerated through a potential of 1kV, and a sputter time of 40 minutes was used. In later cycles, the accelerating potential was lowered to 500V to reduce the depth of sputter damage, while the duration was maintained. After each sputter, the crystal was heated to  $\sim 1000$  K for five minutes, using electron beam heating. After annealing, it would take approximately 30 minutes for the sample to return to room temperature. Following twelve sputter/anneal cycles, LEED was performed to ascertain the condition of the surface. LEED patterns were photographed at four beam energies (figure 8).

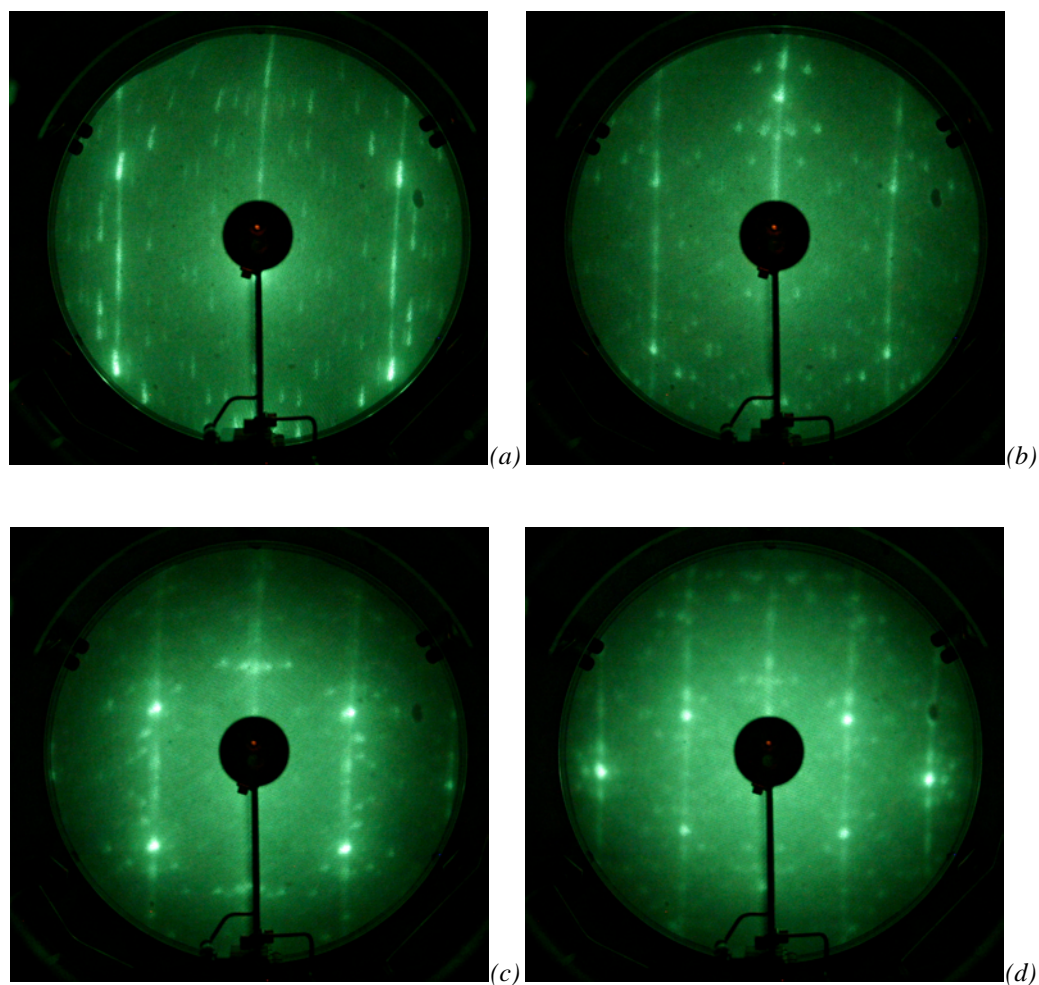


Figure 8. LEED patterns of Cr(110) following twelve sputter/anneal cycles. Beam energies: 54.5eV (a), 75.1eV (b), 112.9eV (c), 164.6eV (d).

Previous studies have observed that new crystals of chromium tend to have a high concentration of carbon, oxygen, and nitrogen in the bulk due to the manufacturing process<sup>29</sup>. Our LEED images (figure 8) do not exhibit the ring-like structures known to be produced by graphitic carbon overlayers. However, they do exhibit two signs of surface impurities—streaks and extra spots.

---

<sup>29</sup> M. Schmid, M. Pinczolics, W. Hebenstreit, and P. Varga, Surf. Sci. **389**, L1140 (1997)

The streaks in the patterns suggest one-dimensional ordering of impurities at the surface. In other words, the lateral interaction between chains of impurity atoms is weak enough to prevent ordering perpendicular to the chains. This aberration may be caused either by disorder in the chromium structure along the  $\langle 110 \rangle$  directions or from domains of impurities that are distributed unevenly along the directions of high symmetry. A previous study of chromium systems found that segregating nitrogen can form a precipitate Cr–N overlayer upon annealing at 450–700°C<sup>30</sup>. Moreover, a herringbone-like structure has been observed in segregating nitrogen systems with domain barriers along the  $[\bar{1}10]$  direction<sup>31</sup>.

The unexpected spots in the pattern can be attributed primarily to impurities rather than defects in the crystal surface. However, it is evident in the higher energy LEED patterns (figure 8.c, d) that these additional spots are distributed symmetrically around the Cr(110) maxima locations. Other LEED investigations have produced similar multiplets on other systems and concluded their existence to be the result of faceting<sup>31</sup>. For single crystal Cr(110), faceting has been observed only for chemisorbed oxygen structures<sup>32,33</sup>.

Therefore, while it is not possible to determine the identities of the present surface impurities without performing auger electron spectroscopy or similar analysis, the deviations from a clear Cr(110) diffraction pattern are consistent with the presence of nitrogen and possibly oxygen but not carbon. Even though the surface suffers from

---

<sup>30</sup> C. Uebing, H. Viefhaus and H. J. Grabke, *Fresenius J. Anal. Chem.* **353**, 254 (1995), *Fresenius J. Anal. Chem.* **346**, 275 (1993)

<sup>31</sup> O. Janzen, C. Hahn, T. U. Kampen and W. Mönch, *Eur. Phys. J. B.* **7**, 1 (1999)

<sup>32</sup> A. Stierle, Th. Koll and H. Zabel, *Phys. Rev. B* **58**, 5062 (1998)

<sup>33</sup> S. Ekelund and C. Leygraf, *Surf. Sci.* **40**, (1) 179 (1973)

substantial contamination, the development of a well-defined pattern and moderate diffuse background intensity attests to reasonable order on the surface.

#### IV. B. Hot-sputtering

Following the assumption that impurities segregating to the surface from within the crystal to be the dominant cause of deviations from a clear LEED pattern, the crystal was bombarded with argon at elevated temperatures to accelerate the removal of these bulk impurities. This process, termed hot-sputtering, allows impurities in the bulk to be segregated to the surface and desorbed through ion interactions, and provides the mobility and space for new impurities to migrate upward in a continuous cycle.

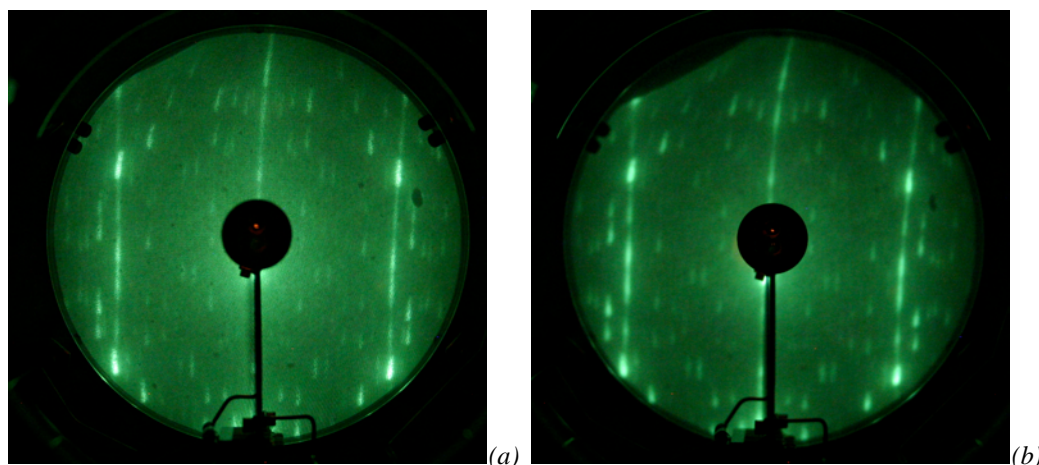


Figure 9. 54.5 eV LEED patterns of Cr(110) before (a) and after (b) hot-sputtering. Note: both images captured using identical shutter speeds.

During each hot-sputter, the pressure of argon in the chamber was  $5 \times 10^{-5}$  Torr. The temperature was held at  $\sim 800$  K, and the bombardment was performed over a thirty minute interval. Following each hot-sputter, the crystal was annealed following the same procedure as in section A. Following this procedure, LEED patterns were obtained at the

same four beam energies previously collected. Diffraction patterns before and after hot-sputtering are presented for an incident beam of 54.5 eV (figure 9).

The resulting patterns showed a reduction in diffuse background as well as an increase in diffraction maxima intensity. The increased gradient between maxima and background bear out the reduction of surface region disorder. However, both the streaks and the secondary spots continue to exist, verifying the persistence of remnant surface, and probable bulk, impurities. The LEED patterns obtained after hot-sputtering at 54.4eV (figure 9.b) and 75.1 eV were converted to a black and white negative including a radial overlay of the off-normal angle below (figure 10) to facilitate cross reference with table 1. It can be seen from these images that the location of diffraction maxima agrees well with our theoretical placement.

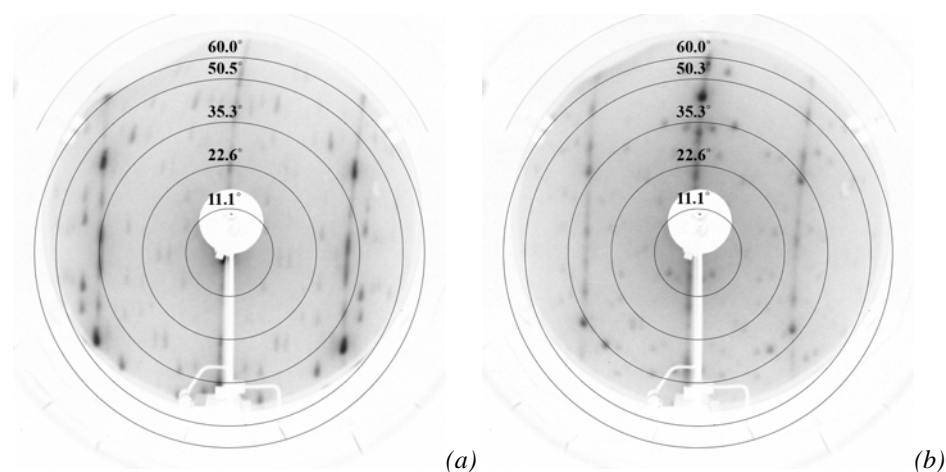


Figure 10. LEED patterns of Cr(110) after hot-sputtering at 54.4 eV (a) and 75.1 eV (b).

## V. Oxide Growth

Even though a completely clean Cr(110) surface region was not obtained, we decided to proceed with the growth of the native oxide. This decision was made due to time constraints as previous studies were besieged by lengthy cleaning efforts<sup>31</sup>. Additionally, a previous investigation of binding interactions found the binding affinity to be stronger for oxygen on chromium than the chromium–nitrogen interaction<sup>34</sup>. Therefore, it was reasonable to assume that the introduced oxygen would replace a large percentage of the nitrogen impurities.

To grow the native oxide, we used the procedure, which was also used by M. Bender *et al.*<sup>16,35</sup>, to provide reasonable comparison of our results with the previously published data. The chamber was backfilled with  $1 \times 10^{-6}$  Torr of oxygen, which was maintained throughout the growth by a variable leak valve and a turbo pump. Using radiative heating from the filament, the crystal was brought to 550 K and held at that temperature for one minute. The crystal temperature was then raised to ~800 K and sustained for two minutes. The crystal was cooled to room temperature with the leak valve to the oxygen off. To remove defects from the oxide, the crystal was annealed at ~1000 K, following the procedure outlined above in the cleaning section. Finally, LEED was performed to determine the crystal structure of the surface (figure 11).

---

<sup>34</sup> C-C Wang, T-H Tang and Y. Wang, *J. Phys. Chem. A*, **104** (42), 9566 (2000)

<sup>35</sup> M. HaBel, Diploma Thesis, Ruhr-Universität, Bochum (1991).

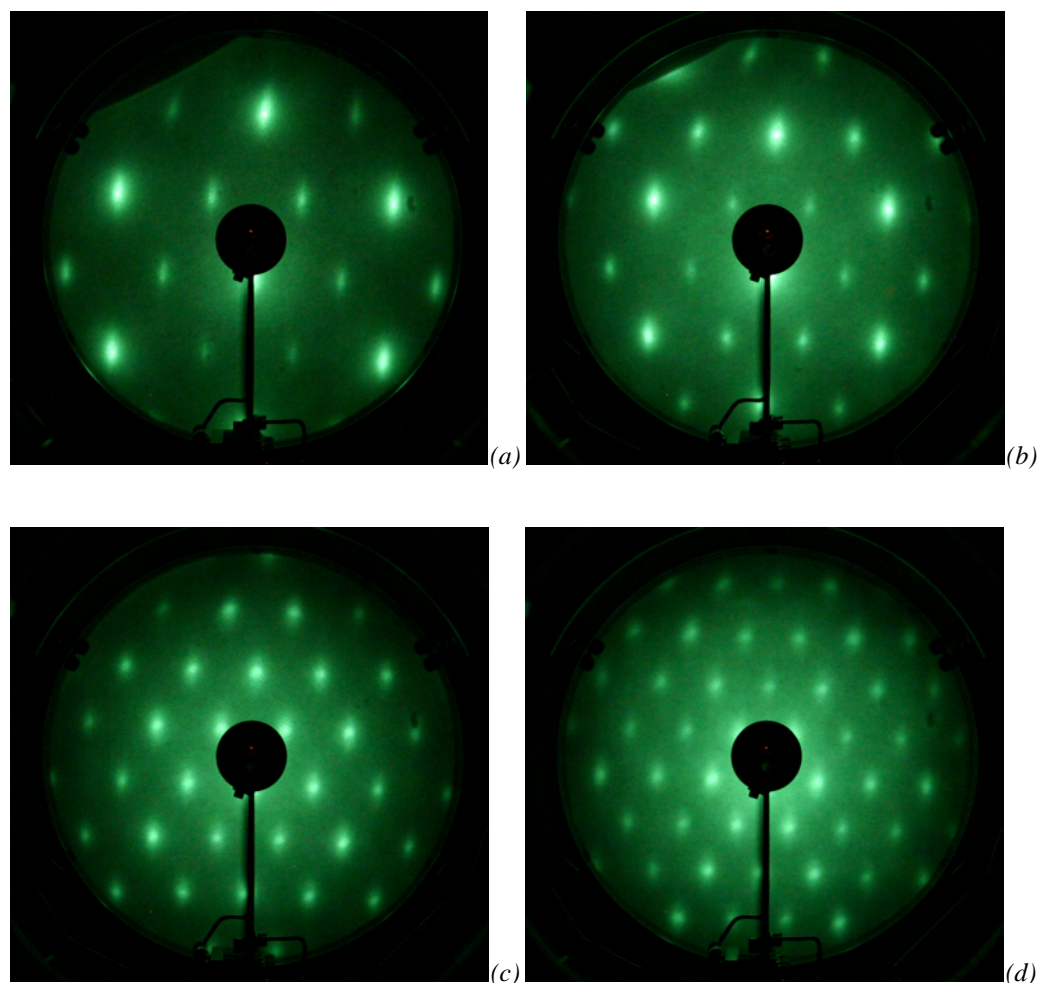


Figure 11. LEED patterns obtained following the growth of  $\text{Cr}_2\text{O}_3(0001)$  on  $\text{Cr}(110)$  at incident beam energies of 54.5eV (a), 75.1eV (b), 112.9eV (c), and 164.6eV (d).

The superposition of the first-order  $\text{Cr}_2\text{O}_3(0001)$  maxima (table 2) and second-order maxima from the oxygen sub-lattice (table 4) is especially evident in figures 11.a and 11.b. The patterns seen in figure 11.a and 11.b have also been converted to black and white negatives including radial overlays of the off-normal angle (figure 12) to facilitate cross-referencing with table 2. It is then shown that the diffraction patterns obtained after growth exhibited the characteristic (1 x 1) pattern of  $\text{Cr}_2\text{O}_3(0001)$ .

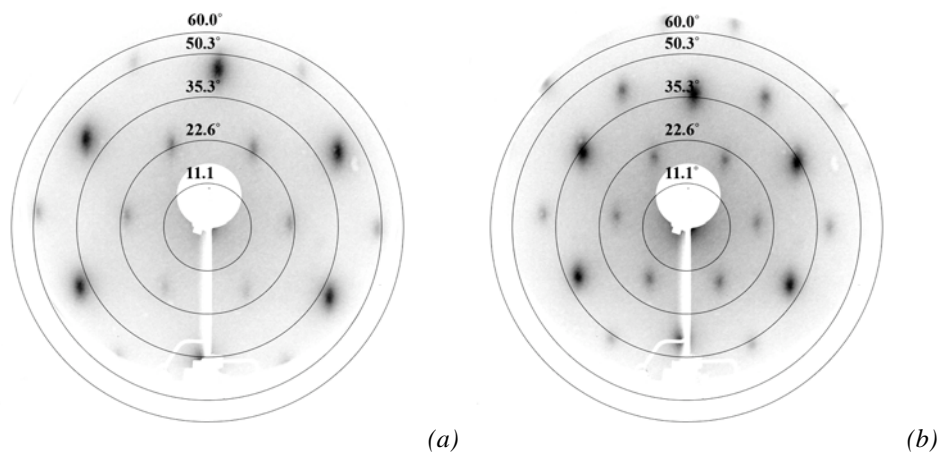


Figure 12. LEED patterns obtained following the growth of a  $\text{Cr}_2\text{O}_3(0001)$  on  $\text{Cr}(110)$  at incident beam energies of 54.5 eV (a) and 75.1 eV (b).

## VI. Analysis of Temperature Dependence

After a  $\text{Cr}_2\text{O}_3(0001)$  overlayer was obtained that exhibited the expected surface geometry, we proceeded with efforts to determine whether a  $(\sqrt{3}\times\sqrt{3})\text{R}30^\circ$  reconstruction could be produced by cooling the crystal. By filling the Dewar with  $\text{LN}_2$ , we were able to cool the crystal through the temperature range where the previous findings reported the transition, allowing the crystal to remain at 140 K for thirty minutes. However, no change in the surface geometry—the diffraction pattern—was observed. We then flashed the crystal to well above previously determined Curie temperature for bulk  $\text{Cr}_2\text{O}_3$ <sup>36</sup>, to ensure that the surface configuration was magnetically stable. LEED patterns for the  $\text{Cr}_2\text{O}_3(0001)$  overlayer at discrete temperatures are shown in figure 13. Additionally, we present Bender *et al*'s published images showing the reconstruction side by side with our results (figure 14).

---

<sup>36</sup> S. Greenwald, *Nature* **168**, 379 (1951)

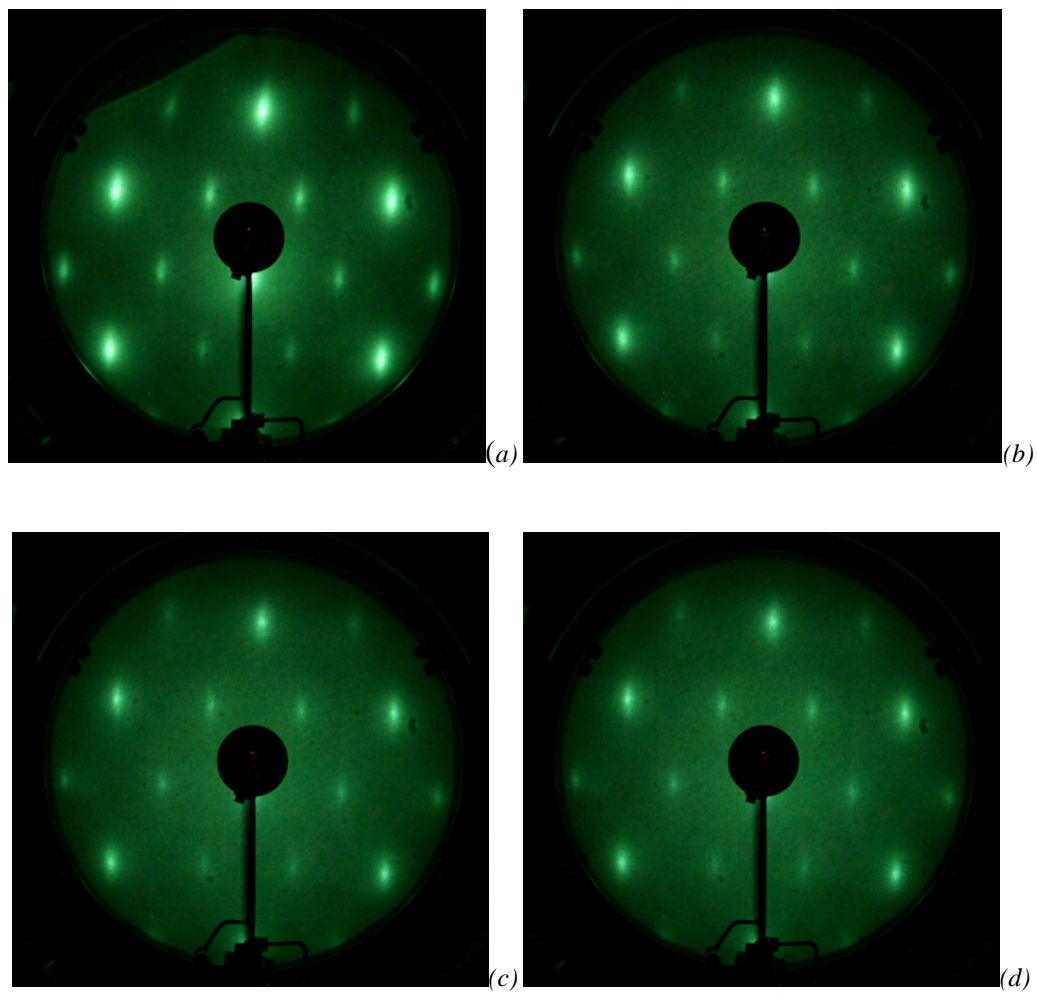


Figure 13. LEED patterns obtained of  $\text{Cr}_2\text{O}_3(0001)/\text{Cr}(110)$  at 300K (a), 175K (b), 140K (c), and 675K (d).

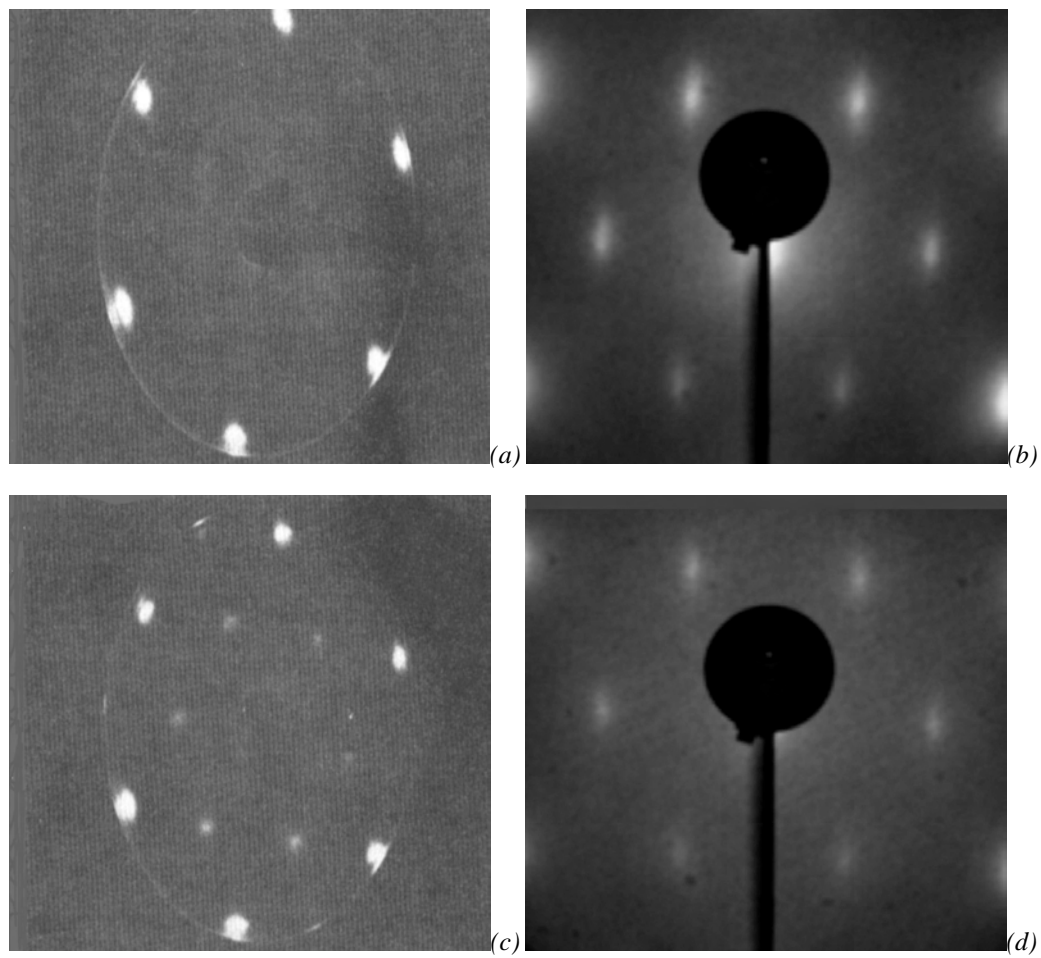


Figure 14. LEED images reported by Bender *et al* at (a) 300 K and (c) 150 K. The diffraction patterns we obtained at (b) 300K and (d) 140 K.

## VII. Conclusions

We have successfully grown a  $\text{Cr}_2\text{O}_3(0001)$  overlayer on  $\text{Cr}(110)$  by vapor phase methods and characterized this surface using LEED. However, investigation of the surface failed to support the previous findings of an induced itinerate magnetic surface reconstruction at low temperatures. This result was not surprising, as magnetic transitions do not commonly vacillate. In matter, magnetism arises from the ordering of internal magnetic dipole moments, which generate net magnetic fields. If the internal entropy of a material is high enough these dipoles will be completely disordered. The temperature above which ordering vanishes for antiferromagnetic coupling is called the Néel temperature, which for  $\text{Cr}_2\text{O}_3$  is  $314 \text{ K}^{38}$ . Because it is typical for the Néel temperature to be different for a thin film system rather than for the bulk material, both groups conclusion of an initial magnetic transition between 175 and 150 K seems, at the outset, reasonable. However, as the temperature continues to decline below the Néel temperature, there should be no further magnetic transformations. It is this later transition at even lower temperatures that makes their conclusions suspect.

Upon comparison of our study with both previous investigations, two disparities emerge. First, prior to growth of the oxide, our  $\text{Cr}(110)$  crystal was beset by surface impurities. However, after the oxide was formed, the LEED pattern was clear, and matched the theoretical calculations of maxima locations. Second, the base pressure in our chamber was  $4 \times 10^{-11}$  Torr, whereas both other groups reported base pressures of  $2 \times 10^{-10}$  Torr, five times higher than ours. It is this discrepancy that motivates our conclusion.

In a previous study<sup>37</sup> where  $\text{Cr}_2\text{O}_3(0001)$  films were prepared on  $\text{Cr}(110)$  in the same manner as in this experiment, the initial adsorption of CO onto the surface was found to occur at 175 K. Furthermore, the CO overlayer was found to order in a  $(\sqrt{3}\times\sqrt{3})\text{R}30^\circ$  pattern relative to the  $\text{Cr}_2\text{O}_3$  layer. Due to the unavoidable presence of carbon monoxide in all vacuum chambers, we believe that the  $(\sqrt{3}\times\sqrt{3})\text{R}30^\circ$  pattern that appears in the clean  $\text{Cr}_2\text{O}_3$  temperature dependence studies is actually the result of residual gases adsorbing on the surface, not a magnetic transition. Because of the reduced quantity of residual gas in our chamber, we did not observe a  $(\sqrt{3}\times\sqrt{3})\text{R}30^\circ$  pattern, likely due to the increased time necessary to form a CO overlayer at our pressure. In addition, the disappearance of the  $(\sqrt{3}\times\sqrt{3})\text{R}30^\circ$  pattern below 150 K is most likely due to the adsorption of  $\text{CO}_2$  (also present in the residual gases of the chamber) which is known to stick on the  $\text{Cr}_2\text{O}_3(0001)$  surface at 135 K<sup>38</sup>.

---

<sup>37</sup> C. Xu, B. Dillmann, H. Kuhlbeck and H-J Freund. Phys. Rev. Lett. **67** (25), 3551 (1991).

<sup>38</sup> S. Funk, T. Nurkic, B. Hokkanen, and U. Burghaus, Appl. Surf. Sci. **253** (17), 7108 (2007).